Evidence for inertia gravity waves forming polar stratospheric clouds over Scandinavia

Andreas Dörnbrack,[1] Thomas Birner,[1] Andreas Fix,[2] Harald Flentje,[2]
Alexander Meister,[2] Heidi Schmid,[2] Edward V. Browell,[3] and Michael J. Mahoney[4]

Received 2 February 2001; revised 25 July 2001; accepted 18 September 2001; published 12 October 2002.

[1] At three successive days at the end of January 2000 the Deutsches Zentrum für Luft- und Raumfahrt (DLR) airborne lidar Ozone Lidar Experiment explored mountain-wave-induced polar stratospheric clouds above the Scandinavian mountain ridge. Global analyses and mesoscale modeling are applied to explain their complex internal structure and their day-to-day variability. Depending on the synoptical-scale meteorological conditions, stratospheric temperature anomalies of different amplitude and horizontal extent are generated by the upward propagating mountain waves. Short-term excitation of about 6 hours resulted in localized stratospheric temperature anomalies directly above the mountain ridge as for 25 January 2000. In this case, the elevation of the observed clouds differed not much from the synoptic-scale clouds upstream above the Norwegian Sea. Onthe other hand, long-lasting flow past the Scandinavian mountain ridge formed huge 400-km horizontally extending stratospheric ice clouds in altitudes as much as 5 km above the elevation of the upstream clouds just 1 day later. Inertia gravity waves with horizontal wavelengths of about 350 km are responsible for their formation. For the first time a predicted temperature minimum far downstream of the mountains could be proofed by the observation of an isolated stratospheric ice cloud above Finland. The observed particles are classified in terms of their measured optical properties such as backscatter ratio and depolarization. In all cases, mountain waves generated ice clouds. In contrast to the nitric acid trihydrate tail of the ice cloud on 25 January the same classification results in a tail of liquid supercooled ternary solutions droplets 1 day later. The particle structure downstream of the mountains is very complex and needs detailed microphyical modeling and interpretation. *INDEX TERMS:* 3329 Meteorology and Atmospheric Dynamics: Mesoscale meteorology; 3334 Meteorology and Atmospheric Dynamics: Middle atmosphere dynamics (0341, 0342); 3337 Meteorology and Atmospheric Dynamics: Numerical modeling and data assimilation; 0305 Atmospheric Composition and Structure: Aerosols and particles (0345, 4801); *KEYWORDS:* Polar stratospheric clouds, inertia gravity waves, mountain waves, mesoscale numerical modelling, Lidar observations

Citation: Dörnbrack, A., T. Birner, A. Fix, H. Flentje, A. Meister, H. Schmid, E. V. Browell, and M. J. Mahoney, Evidence for inertia gravity waves forming polar stratospheric clouds over Scandinavia, *J. Geophys. Res.*, *107*(D20), 8287, doi:10.1029/2001JD000452, 2002.

1. Motivation

[2] There is now substantial evidence for the crucial role of polar stratospheric cloud (PSC) particles in the heterogeneous conversion of inert reservoir gases to photochemically active species, which drives the catalytic ozone destruction cycle. These stratospheric clouds consist either of water ice particles (PSCs of type II also called mother-of-pearl clouds), solid nitric acid trihydrate ($HNO_3 - 3 \cdot H_2O$, NAT; PSCs of type Ia), or liquid supercooled ternary solutions ($HNO_3/H_2SO_4/H_2O$ STS; PSCs of type Ib). For a given mixing ratio of water vapor and nitric acid, PSCs form if the local temperature falls below one of the threshold values $T_{NAT} > T_{STS} > T_{frost}$ [*Hanson and Mauersberger*, 1988]. Typical values for the threshold temperatures at 30 hPa are 192, 188, and 185 K assuming volume mixing ratios of 5 ppm for water vapor and 10 ppb for NAT. The actual formation process of the different PSC particles is still a matter of debate [*Peter*, 1997; *World Meteorological Organization*, 1999].

[3] PSCs form on large spatial scales (synoptic scale) and on mesoscale and local scales due to different cooling mechanisms. Synoptic-scale PSCs occur if the air inside the polar vortex cools below the formation temperatures. The Arctic stratosphere, however, is disturbed by transient

[1]Deutsches Zentrum für Luft- und Raumfahrt (DLR) Oberpfaffenhofen, Institut für Physik der Atmosphäre, Wessling, Germany.
[2]Deutsche Luft-und Raumfahrt Oberpfaffenhofen, Lidar Gruppe, Wessling, Germany.
[3]Lidar Application Group, Atmospheric Science Research, NASA Langley Research Center, Hampton, Virginia, USA.
[4]Jet Propulsion Laboratory, California Institute of Technology, Pasadena, California, USA.

0148-0227/02/2001JD000452$09.00

planetary waves and the polar vortex is often deformed and asymmetric. Thus the stratospheric air is frequently too warm for the formation of PSCs on the synoptic scale [e.g., *Pawson et al.*, 1995].

[4] Upward propagating mountain waves are able to generate stratospheric temperature anomalies by adiabatic cooling of rising air parcels. Thereby mesoscale PSCs can form which are important for two reasons. First, they constitute localized regions of chlorine activation (''cold processing'') above and in the lee of mountain ranges like those in Greenland and Scandinavia [*Carslaw et al.*, 1998a, 1998b] even if the synoptic-scale temperature is too high. Second, owing to their limited extent (typically as much as 350 km), their stationarity over several hours, and their good predictability [*Eckermann et al.*, 2002] mountain-wave-induced PSCs are an ideal natural laboratory for the study of the formation and dissipation of cloud particles. Therefore one of the objectives of the international campaign Stratospheric Aerosol and Gas Experiment (SAGE III) Ozone Loss and Validation Experiment/Third European Stratospheric Experiment on Ozone (SOLVE/THESEO-2000) was to explore the spatial and temporal structure of mountain-wave-induced polar stratospheric clouds.

[5] Mountain-wave-induced PSCs in northern Scandinavia form mainly under foehn-like weather conditions. Early observations of mother-of-pearl clouds in northern Scandinavia reveal a strong correlation between their appearance during the polar night and deep surface pressure lows passing the Norwegian Sea toward the northeast [*Störmer*, 1929, 1934]. For example, *Dietrichs* [1950] concluded that in more than 75% of 96 visual observations over a 60-year period the low-altitude wind speed on the upstream side was high and the wind was from the west-northwest. This indicates that the formation of PSCs is correlated with strong flow across the Scandinavian mountain range. Recent in situ and remote sensing observations of PSCs above Scandinavia confirm this close relationship [*Enell et al.*, 1999; *Wirth et al.*, 1999; *Dörnbrack et al.*, 1999; *Voigt et al.*, 2000].

[6] Balloonborne and in situ aircraft observations of PSCs are rare. Most often, conclusions concerning the whole air mass are drawn from single measurements. Lidar instruments offer the unique possibility to explore the vertical and horizontal structure of PSCs. For example, onboard aerosol lidar systems may be used to measure backscatter from PSCs and study any differences in the PSC structure upstream and downstream of the mountains.

[7] This paper concentrates on a comprehensive description of a mesoscale mountain wave event that occurred over northern Scandinavia during the second deployment of the SOLVE/THESEO-2000 campaign at the end of January 2000. Based on global and mesoscale stratospheric forecasts, several observations were made to measure mountain-wave-induced PSCs above northern Scandinavia during a period of three consecutive days. Here mainly lidar observations onboard the Deutsches Zentrum für Luft- und Raumfahrt (DLR) Falcon and the NASA DC-8 are used. For the first time, lidar observations give strong evidence of inertia gravity waves forming PSCs in the lee of the Scandinavian mountains. Additionally, global analyses and mesoscale modeling are applied to understand and explain the individual measurements.

[8] The paper is organized as follows: in section 2 we briefly describe the instruments and numerical tools. Section 3 gives an overview of the synoptic situation during the mountain wave event. Section 4 presents the results, and section 5 concludes the paper with a discussion of the results.

2. Instruments and Tools

2.1. Lidar Instruments

[9] Results of two different lidar systems are presented in the following. Onboard the DLR Falcon F-20 aircraft, the biaxial Ozone Lidar Experiment (OLEX) [*Moerl et al.*, 1981; *Wirth and Renger*, 1996; *Flentje et al.*, 2000] uses the fundamental, frequency doubled, and tripled light of a neodymium:yttrium/aluminum/garnet (Nd:YAG) laser corresponding to wavelengths of 1064, 532, and 355 nm. The backscattered radiation is received by a 35-cm diameter Cassegrain telescope. With a repetition rate of 10 Hz for a typical aircraft speed of 200 m s^{-1} the raw data resolution is about 20 m in the horizontal dimension. In the vertical dimension the analog-to-digital converter sampling rate results in a resolution of 15 m. The single profiles are averaged horizontally and vertically, resulting in a trade-off between error and spatial resolution.

[10] The total aerosol backscatter ratio, denoted by γ, is defined as the ratio of the total backscatter coefficient to the molecular backscatter coefficient $\gamma = (\beta_{aerosols} + \beta_{molecules})/\beta_{molecules}$. For the inversion of the β profiles the standard Klett method is applied [*Klett*, 1985]. From the backscatter coefficients at the three wavelengths two color ratios are derived as indicators for the optically dominant particle sizes. The aerosol depolarization ratio at 532 nm $\delta_{532} = \beta_{aerosols,\perp}/\beta_{aerosols,\parallel}$, where $\parallel$ and $\perp$ stand for parallel and perpendicular polarized light, provides information on aerosol shapes, permitting the distinction between liquid and solid aerosols.

[11] On the NASA DC-8 the UV Differential Absorption Lidar (DIAL) system is used to measure aerosol, cloud, and ozone profiles above the aircraft [*Browell et al.*, 1998; *Grant et al.*, 1998]. A pair of Nd:YAG and Nd:YAG-pumped dye lasers are employed to generate wavelengths near 1064, 620, 600, 310, and 300 nm. Here only the infrared wavelength is used to determine the aerosol scattering ratio profile. The vertical data resolution is 150 m and the horizontal running average interval is 30 s (7 km at DC-8 speed of 14 km min^{-1}). All measurements reported in this text are made along flight segments which are oriented nearly parallel to the predicted mean stratospheric wind field.

2.2. Microwave Temperature Profiler

[12] The Jet Propulsion Laboratory DC-8 Microwave Temperature Profiler (MTP) is a passive microwave radiometer that measures the natural thermal emission from oxygen molecules at three frequencies (55.51, 56.66, and 58.79 GHz). The instrument looks at 10 elevation angles between −80 and +80 by using a scanning mirror (located behind a microwave window on the sensor unit) to change the viewing direction. Measured brightness temperature versus elevation angle is converted to air temperature versus altitude using a modified statistical retrieval procedure. Temperature profiles are obtained every 15 s, corresponding

to 3.5 km horizontal resolution at typical DC-8 speeds; the vertical resolution is 300 m near the aircraft and degrades with distance above and below. The temperature field is used to derive the altitudes of isentrope surfaces to look for the presence of atmospheric waves [*Gary*, 1989].

2.3. Meteorological Modeling

[13] Daily ECMWF analyses serve to characterize the synoptic-scale state of the atmosphere. The six hourly data are stored on a regular latitude/longitude grid with a spatial resolution of 0.5° and with 60 model levels from the surface up to 0.1 hPa.

[14] The mesoscale fields are calculated with the non-hydrostatic weather prediction model MM5-version 3 [*Dudhia*, 1993; *Dudhia et al.*, 2001]. The model setup consists of three domains, where the outer model domain is centered around (65°N, 15°E) with an extension of 2184 km × 2184 km. In this domain a horizontal grid size of Δx = 24 km is used. A local grid refinement scheme (nested domains of 8 and 2.67 km horizontal resolution) is applied to resolve most of the horizontal wave number spectrum of vertically propagating gravity waves excited by the orography.

[15] In previous simulations and partly due to the lack of stratospheric analyses the model top was set to 10 hPa (≈28 km), where a radiative boundary condition avoids the reflection of vertically propagating waves of wavelengths less than $12\Delta x$ [*Zängl*, 2002]. For longer gravity waves for which the horizontal component of group velocity is non-zero, some of our previous results might have been influenced by partial reflection at the model top. This is critical if the simulated structures are closely beneath the model top like polar stratospheric clouds at heights above 24 km.

[16] The mesoscale simulations presented in this paper are performed with 65 levels up to the model top at 5 hPa (≈32 km) which results in a vertical resolution of approximately 500 m. More important, a modified radiative top boundary condition introduced by *Zängl* [2002] is applied for the simulations. This boundary condition successively interpolates the spectrum of radiated waves from the outer to the inner domains. It thus avoids the reflection of waves less than $12\Delta x_{\text{outerdomain}}$ = 288 km throughout all domains. The contamination of results by reflected modes in the height interval of the lidar observations is therefore reduced. Radiative and moist processes are switched off since the prime concern lies in the dynamics of mountain waves at upper levels. The initial conditions and boundary values of the model integration were prescribed by 6 hourly analyses of the European Centre for Medium-Range Weather Forecasts (ECMWF) with a horizontal resolution of 0.5° in latitude and longitude and 18 pressure levels between the surface and the 5-hPa pressure level.

3. Meteorological Situation

[17] The observations discussed in this paper were carried out on three consecutive days: 25, 26, and 27 January 2000. On all these days, mother-of-pearl clouds (ice PSCs) could be observed visually and by remote and in situ sensors above northern Scandinavia. All observations indicate mountain waves as the primary cause for their formation. On 25 January 2000, PSCs were investigated on three platforms flying above and in the lee of the Scandinavian mountain range: on NASA DC-8, by DLR Falcon, and by the PSC analysis balloon [*Voigt et al.*, 2000]. On 26 January 2000 only the DLR Falcon was in operation and traversed the Scandinavian mountain ridge twice to survey the large extent of mountain-wave-induced PSCs. Finally, on 27 January 2000 the DLR Falcon flew simultaneously with the TRIPLE gondola above northern Scandinavia [*Schiller et al.*, 2002]. The DC-8 flew on this day over southern Scandinavia and the MTP sensor showed gravity wave activity above the mountain range.

[18] Figure 1 shows the geopotential height of the 850 hPa surface and the corresponding horizontal wind at 1200 UT in the period from 24 to 27 January 2000. The synoptic evolution in the troposphere is characterized by stationary high mean sea level pressure (a blocking high and following a high-pressure ridge) over the Atlantic Ocean and a sequence of deepening low-pressure systems (minimum core surface pressure: 980 hPa on 25 January, 966 hPa on 26 January, and 964 hPa on 27 January) traveling east toward the Barents Sea. On the rear side of these storms, the near-surface wind intensified and turned from southerlies to westerly winds blowing nearly perpendicularly across the mountain ridge on 25 and 26 January (see the 850 hPa wind in Figures 1b and 1c). On 27 January the near-surface wind turned to northerlies and became weaker. During the whole period, gravity waves were excited by the flow across the mountain ridge.

[19] Figure 2 shows the evolution of the polar vortex in terms of potential vorticity on the 475 K isentrope during this period. The potential vorticity is calculated by means of the global ECMWF analyses. The temperature on the 30-hPa surface and the geopotential height for the southeast section of the vortex are shown in Figure 3. Here the respective aircraft flight legs and the balloon trajectories are indicated. All observations were performed close to the southern edge of the polar vortex. Generally, the polar vortex was stable and coherent during the winter of 1999/2000 [*Manney and Sabutis*, 2000]. During the considered period the position of its edge relative to Scandinavia moved southward. Due to this development, upper tropospheric and lower stratospheric winds (compare geopotential at 30 and 850 hPa, Figures 1 and 3) were aligned with the winds at launch height of the gravity waves.

[20] Table 1 shows that the horizontal wind speed at 850 hPa normal to the Scandinavian mountain ridge increases steadily until 26 January 0000 UT and decreases after this date until the end of the considered period. The values are taken from ECMWF analyses at a typical upstream location (68°N, 10°E). The horizontal wind speed near the tropopause (200 hPa) is close to and larger than 50 m s^{-1} until 26 January 0600 UT. Generally, the directional shear in troposphere never exceeds 55°. However, small values of $\Delta\alpha <$ 15° indicate the most favorable conditions for wave propagation in the morning hours of 25 and 26 January. On the latter day the near-surface wind speed is up to 50% larger than on 25 January. Therefore, gravity waves excited by the strong flow past the Scandinavian mountain ridge could propagate without significant absorption into the stratosphere. A similar synoptic situation occurred in the winter of 1996/1997 [*Dörnbrack et al.*, 2001].

[21] On the synoptic scale the stratospheric temperature inside the vortex was below T_{NAT} = 192 K (blue region in

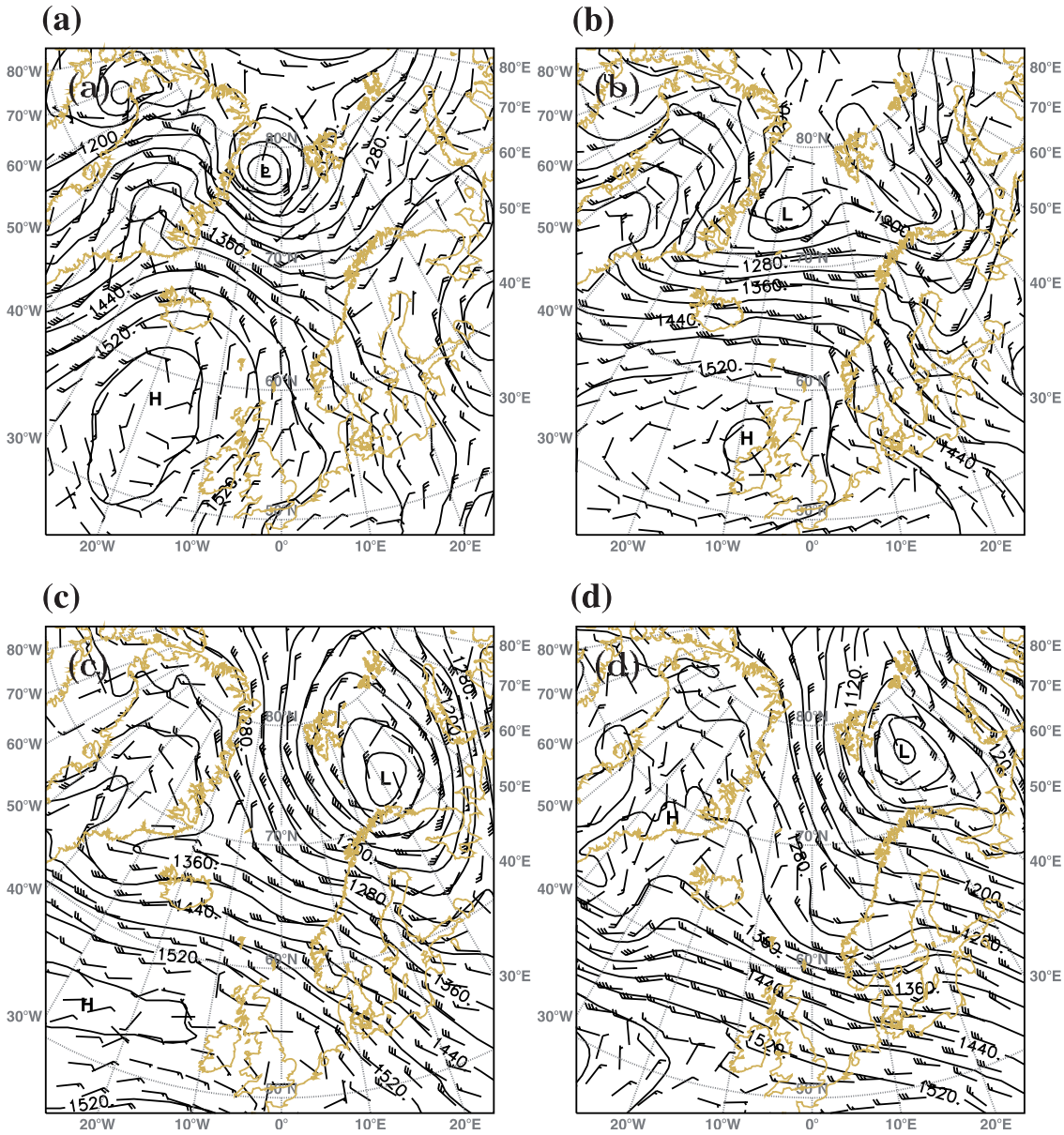

Figure 1. Geopotential height (in meters) and wind (a full barb represents a wind speed of 5 m s^{-1}, a half barb that of 2.5 m s^{-1}, and a pennant a wind speed of 25 m s^{-1}) at 850 hPa at 1200 UT on (a) 24 January, (b) 25 January, (c) 26 January, and (d) 27 January 2000. ECMWF analyses at 0.5° × 0.5° horizontal resolution.

Figure 3) during this period. Above Scandinavia, mountain waves dropped the temperature below T_{frost} = 188 K on 25 and 26 January. It should be noted that the mesoscale features are already analyzed by the current ECMWF model with 0.5° × 0.5° horizontal resolution. Additional mesoscale simulations presented in the following sections will confirm and provide details to the ECMWF analyses.

4. Observations

[22] This section presents chronologically observations of mountain-wave-induced PSCs above northern Scandinavia in the period from 25 to 27 January 2000. The observations along with results from mesoscale model simulations are used to highlight the PSC characteristics including structure and variability. The optical properties are discussed in section 5.

4.1. Period 25 January 2000

[23] Figure 4 shows horizontal sections of the simulated temperature field at 21 and 23 km above the observation area on 25 January 2000 at 1600 UT. This area represents the innermost model domain (horizontal mesh size of 2.67 km) above northern Scandinavia of a mesoscale simulation initialized at 0600 UT. In the period from 1200 UT to 1800 UT, both the mesoscale model simulation and the global ECMWF analyses calculate a significant amplification of the mountain-wave-induced temperature anomaly (not shown).

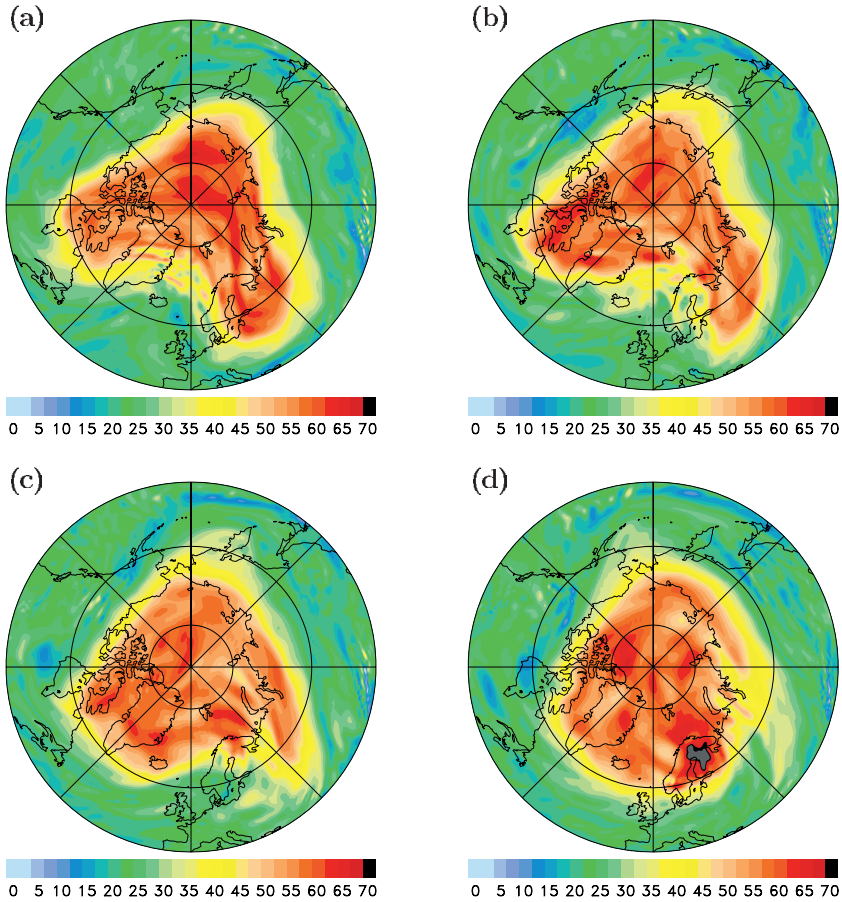

Figure 2. (a–d) Potential vorticity (10^{-6} km^2 s^{-1} kg^{-1}) at the 475 K isentrope from 24 to 27 January 2000 at 1200 UT. Polar stereographic projection of the Northern Hemisphere whereby the outer border is at 40°N. ECMWF analyses at 0.5° × 0.5° horizontal resolution.

[24] Above the mountain ridge there is a coherent cold region with temperatures below 190 K extending from 21 to about 25 km (compare Figure 5). On its upwind side there is a sharp horizontal temperature gradient, whereas the temperature increases more gradually on the downwind side (see temperature field at 23 km). At 23 km altitude the simulated stratospheric temperature drops below 185 K, permitting the formation of ice particles. In addition to the mesoscale temperature anomaly with a horizontal extension in mean flow direction of about 200 km, there are smaller scale structures with horizontal wavelengths of less than 20 km. These waves produce temperature anomalies of similar amplitude and appear predominantly at 21 km, that is, near the lower edge of the temperature anomaly. The simulated lifetime of the mesoscale temperature anomaly is about 8 hours. Visual observations on this day in Kiruna confirm an apparent wave structure of tropospheric as well as stratospheric clouds from about noon until dusk (at about 1600 UT). During this entire period a strong westerly wind blew steadily and grew weaker in the evening hours.

[25] Figure 5 shows the aerosol backscatter ratio γ along the longest cross-mountain flight leg of the DLR Falcon at about 1530 UT. The cross section lies in a west-east direction and the MM5 temperature and potential temperature are superimposed. Between 22 and 24 km there is a layer of high backscatter ratio γ >100 extending from the peak of the mountain range at about 19°E downstream to 21°E. This is an ice PSC with a horizontal extension of about 120 km. An aerosol layer with backscatter ratios of less than 30 surrounds the PSC and extends further downstream to the Baltic Sea. The downstream layer contains isolated thin layers of γ >100. Unfortunately, there is no lidar observation by DLR Falcon upstream of the mountains on this day.

[26] There are two remarkable features of this PSC observation. First, the core of the PSC with high γ-value is nearly horizontal and starts abruptly above the highest mountains. However, the short observation upstream of the cloud shows steep ascending aerosol layers with $\gamma \approx 2\ldots5$. On the lee side of the mountains, the descending PSC layer is characterised by larger backscatter ratios of $\gamma \approx 10$. Secondly, there is a significant difference in the cloud shape at its upper and lower edge. The undulations at the lower edge have a typical wavelength of about 20 km whereas the waves at the upper edge are shorter and much more regular (it should be noted that Figure 5 does not show the true length-to-height ratio).

[27] The simulated temperature structure predicts a cold layer with T < 185 K inside the observed PSC area (Figure 5, top). At the upstream edge of the cloud the temperature drops below 182 K. Whereas at the upper cloud edge the

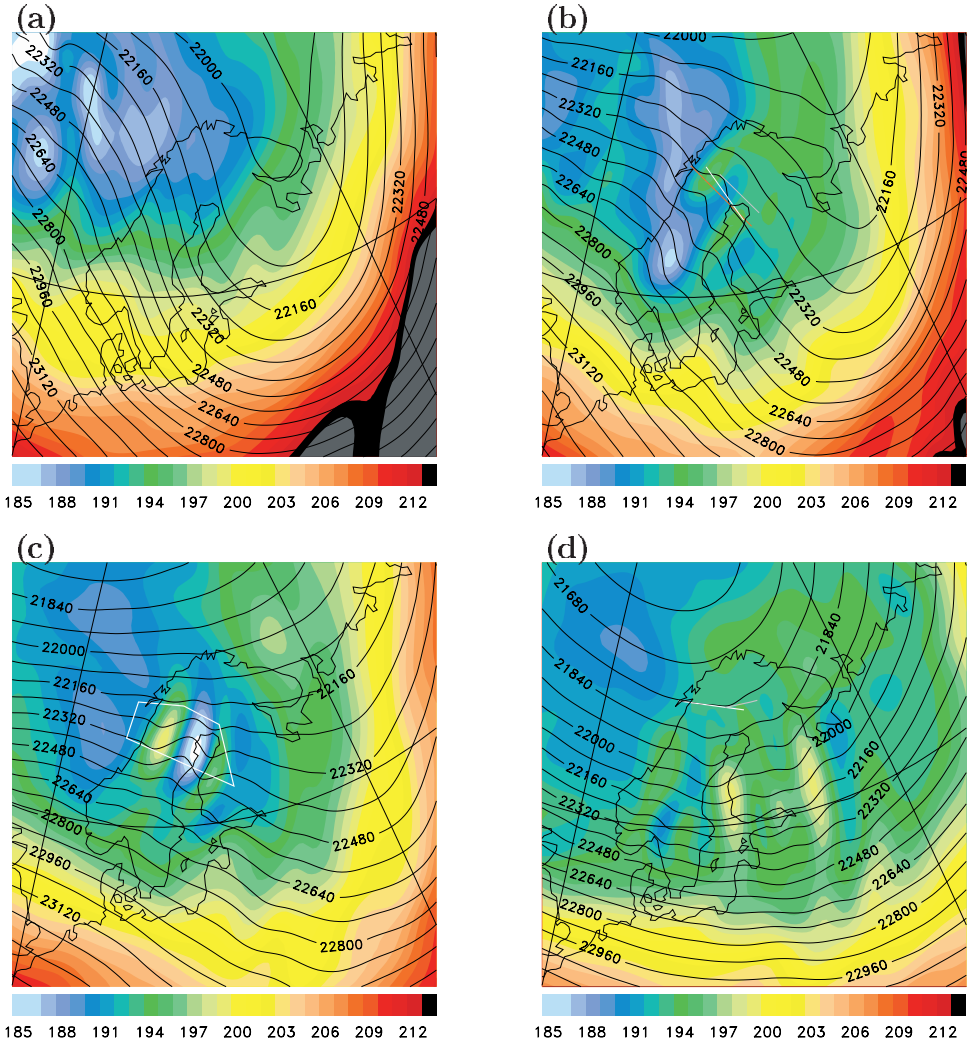

Figure 3. (a–d) Temperature (K) and geopotential height of the 30-hPa surface from 24 to 27 January 2000 at 1200 UT. White lines, DLR Falcon flight tracks for which lidar observations are presented; grey lines, balloon trajectories (PSC analysis 25 January; TRIPLE 27 January); red line, section of the DC-8 flight leg on 25 January 2000 shown in Figure 6. ECMWF analyses at 0.5° × 0.5° horizontal resolution.

small-scale undulations cannot be represented by the simulation, the model is able to reproduce effectively the overall shape of the observed structure. Above the cloud a strong inversion with a temperature gradient of about +15 K/km at about 24 km altitude exists in the model results.

[28] The cross-section of potential temperature (Figure 5, middle) helps to explain the observed and simulated structure. Upstream of the mountains the isentropic surfaces are nearly horizontal. Directly above the highest mountains the isentropes are vertically displaced due to the mountain waves. The cooling due to adiabatic expansion of air parcels flowing along upward bended isentropes produce the sharp upstream edge of the observed PSC. Another region with steep and overturing isentropes is simulated directly above the observed cloud and predominantly between the peak of the ridge and Kiruna (marked by the vertical line in Figure 5). The inspection of former simulation times gives evidence that this is a wave-breaking region with local Richardson numbers close to and less than zero.

[29] As the horizontal wind speed is nearly zero in this wave breaking region, a self-induced critical layer forms. A

Table 1. Upstream Values at 68°N and 10°E

Date/Time UT	$V_\perp$ (850 hPa)	V_H (200 hPa)	$\Delta\alpha$	Barcode
2000012400	10.4	56.7	23.0	Y
2000012406	4.8	78.7	13.8	N
2000012412	10.6	53.4	46.4	N
2000012418	14.6	47.9	54.6	N
2000012500	15.5	47.2	13.0	Y
2000012506	16.5	49.1	3.6	Y
2000012512	18.8	51.7	31.9	N
2000012518	17.1	57.4	19.0	Y
2000012600	24.2	53.5	7.1	Y
2000012606	22.6	52.1	14.4	Y
2000012612	16.3	37.3	18.2	Y
2000012618	15.6	30.9	28.9	Y
2000012700	13.3	27.0	16.2	Y
2000012706	12.4	27.9	17.1	Y
2000012712	11.7	20.2	17.1	Y
2000012718	11.1	19.5	36.4	N

$V_\perp$ is the horizontal wind speed at 850 hPa perpendicular to the Scandinavian mountain ridge, V_H is the horizontal wind speed at 200 hPa, and $\Delta\alpha$ is the directional shear between the 850 and 200 hPa level. The velocities are in m s^{-1}, and the angle is in degrees. The column Barcode indicates dates with significant stratospheric mountain wave activity (Y, yes; N, no) according to the criteria by *Dörnbrack et al.* [2001].

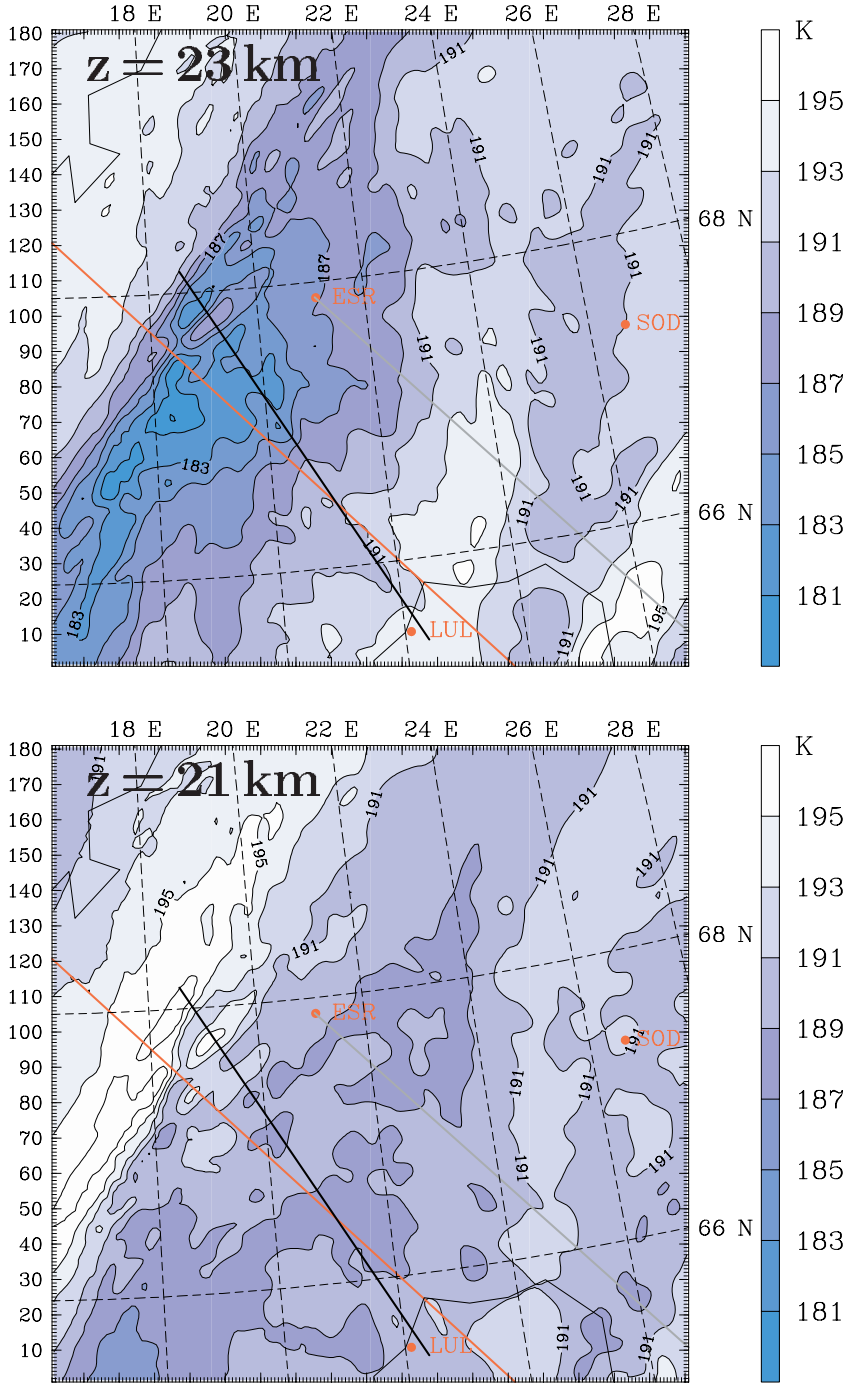

Figure 4. Temperature at 21 and 23 km on 25 January 2000 at 1600 UT (+10 hours). Results from the innermost model domain of the MM5 simulation. The PSC analysis balloon trajectory and the cross-mountain flight legs of the DLR Falcon and NASA DC-8 are indicated by solid gray, black and red lines, respectively. The distance between two small tick marks along the perimeter equals the horizontal grid size of 2.67 km.

critical layer is defined as the location where the phase speed of the gravity waves equals the mean flow speed, that is, for mountain waves where the horizontal wind speed is zero [*Booker and Bretherton*, 1967; *Baines*, 1995]. This layer inhibits the further vertical propagation of gravity waves excited by the flow over topography. Directly beneath the breaking region a stably stratified layer with dense isentropes exists across the upper edge of the observed cloud. The thickness of this layer is about 1.5 km. Due to the strong vertical shear of the horizontal wind speed, Kelvin-Helmholtz waves are likely to develop. The observed wavelength of the undulations at the upper cloud edge is less than 10 km and their amplitude is about 200 m. Thus the theoretically predicted range of wavelengths of the Kelvin-Helmholtz

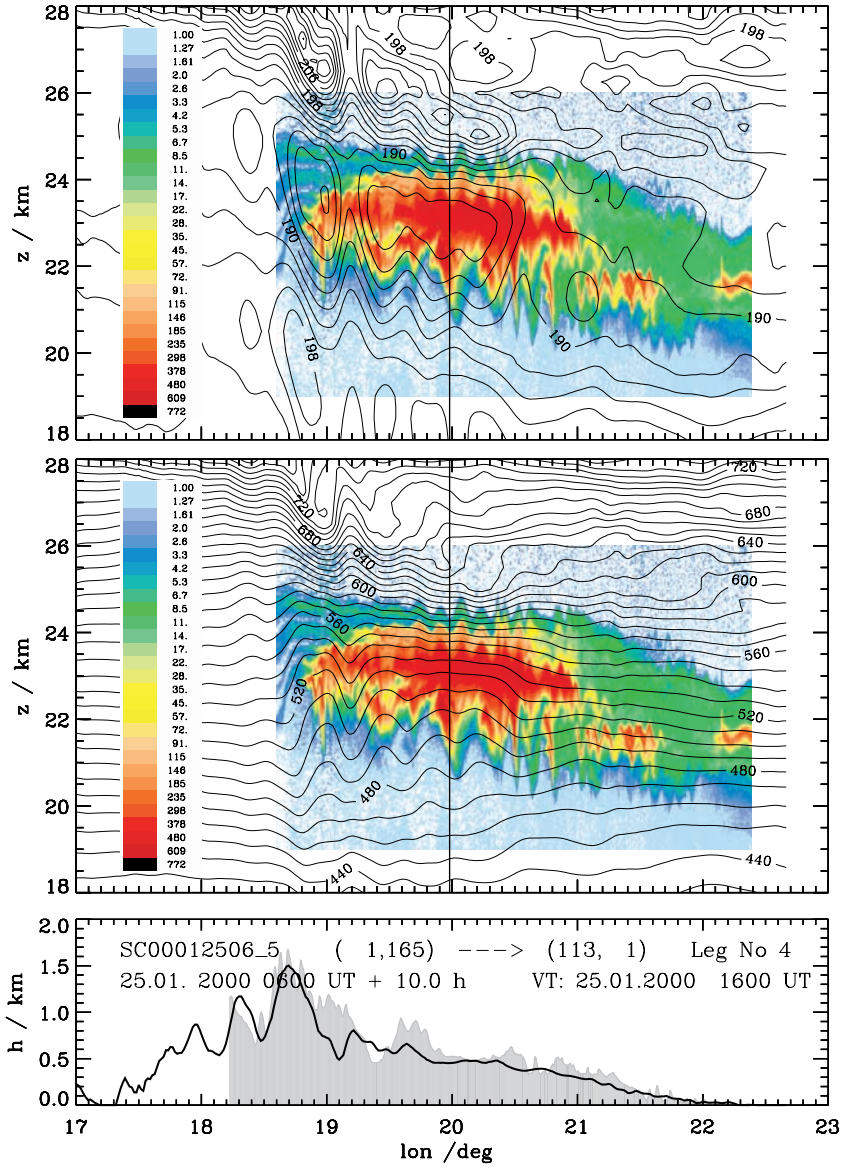

Figure 5. Backscatter ratio γ at 1064 nm along the flight track of the DLR Falcon on 25 January 2000 from 1510 to 1540 UT (color shading top panels). (top) Superimposed are the MM5 temperature (2 K interval) and (middle) potential temperature (10 K interval) along the flight track at 1600 UT (+10 hours). The vertical line marks the position of Kiruna. (bottom) Elevation of the topography below the flight leg (gray shading; digital topography in 1 km horizontal resolution; black line, topography in the innnermost nested domain of MM5).

waves of 4.4–7.5 times the thickness of the layer (6.6–11.2 km) agrees with the observed horizontal wavelength. The mesoscale model with the current horizontal and vertical resolution cannot resolve such small-scale features. However, the background conditions favorable for shear instability are well simulated. In this way, the nearly sinusoidal undulations on the upper edge of the PSC can be understood as being generated by shear instability.

[30] Another nearly simultaneous PSC observation of this day is shown in Figure 6. NASA's DC-8 crossed the mountains south of DLR Falcon about 1 hour later. Fortunately, its lidar observations partly cover the conditions upstream of the mountain ridge. A composite of DC-8 DIAL observations and MTP-retrieved isentropic surfaces is compared with the model results of the innermost domain.

[31] The striking feature of the stratospheric MTP observations are the large vertical displacements of isentropes at all levels above the highest mountain peak below the flight path. Maximum displacements of about 1000 m have been determined. The observed horizontal wavelength is about 30 km. The vertical wavelength deduced from numerical simulations is about 8 km. This gives an aspect ratio (vertical to horizontal scale) of less than 1. According to the terminology of *Gill* [1982], this is a nonrotating hydrostatic gravity wave. The linear dispersion relation for these waves predicts that the vertical and horizontal wave number are independent and that all the energy propagates verti-

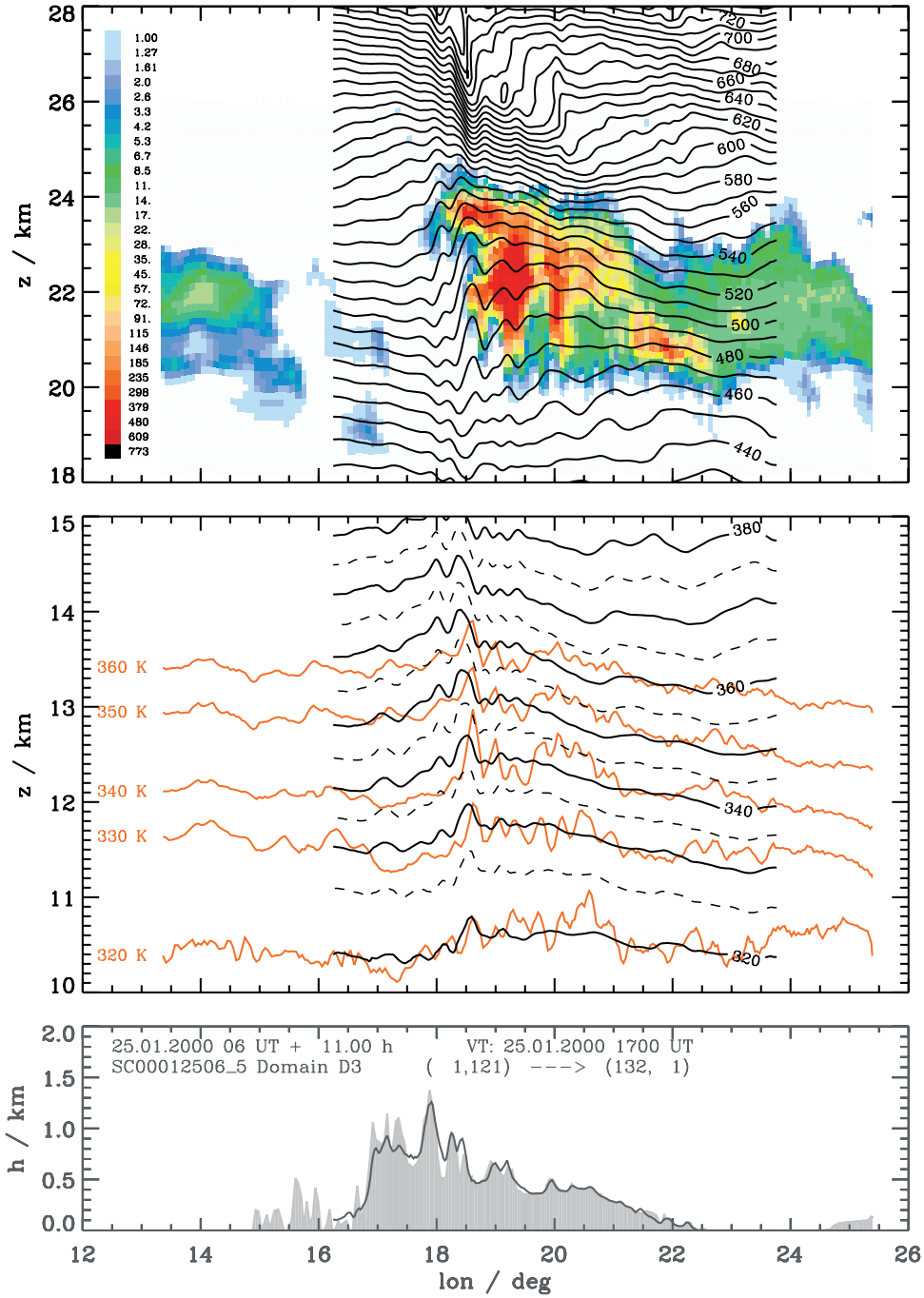

Figure 6. (top) NASA DC-8 DIAL zenith aerosol scattering ratio $\gamma - 1$ at 1064 nm along the flight track indicated in Figure 4. Superimposed is the MM5 potential temperature along the flight track at 1700 UT (+11 hours). (middle) Isentropes derived from the MTP sensor on board NASA DC-8 (red). Superimposed is the MM5 potential temperature along the flight track at 1700 UT (+11 hours). (bottom) As in Figure 5.

cally. The simulated isentropes show a close agreement with the observed position of maximum displacements and the wave amplitude at 320 K. At higher vertical levels the simulated isentropes are slightly more tilted than the measured ones. The breaking region above the cloud is not completely resolved by the mesoscale model. Therefore reflected modes, which lead to smaller tilts, are not fully represented by the model. However, the simulated amplitudes are quite similar to the observed ones, although, as mentioned before, the observed smaller scale structures are not resolved by the numerical model. Furthermore, the distance between the isentropic surfaces (the stability above the tropopause) is well represented by the numerical simulation.

[32] The amplitude of the vertically propagating gravity wave amplifies in the stratosphere and peak-to-peak ampli-

tudes of about 1500 m (see the 510 K isentrope in Figure 6) are simulated. Assuming dry adiabatic expansion, this is nearly equivalent to a local cooling of about 15 K. At the position of maximum adiabatic cooling a PSC layer forms between 21 and 23 km with aerosol scattering ratios γ_{1064} greater than 100. At 24 km, where the isentropes are less steep, a more gradual transition to a high backscattering region is observed. Similar to the DLR Falcon observations, the ice cloud extends downstream about 150 km and is followed by an aerosol layer with smaller backscatter ratios. This layer encloses isolated patches with high γ_{1064} values at lower altitude similar to those observed by DLR Falcon some kilometers to the north.

[33] Upstream of the mountains above the Norwegian Sea, an aerosol layer with scattering ratios of up to 30 has been measured at around 22 km. Due to the wave-induced descent of isentropes the aerosol particles evaporate and create an almost cloud-free column in front of the mountain range.

[34] At 2000 UT of this day the PSC analysis payload was launched at Esrange (68°N, 21°E) under nearly windless conditions. The balloon trajectory is indicated in Figure 4. A vertical section along this trajectory shows a cold, almost 3-km-thick PSC layer at 21 km around 250 km downstream of the mountains [*Voigt et al.*, 2000]. The in situ measurements onboard the gondola allowed a detailed analysis of the complex PSC composition in the lee of the mountains [*Schreiner et al.*, 2002; *Larsen et al.*, 2002]. Here in section 5 we only present the classifications based on the airborne lidar observations.

4.2. Period 26 January 2000

[35] During the night from 25 to 26 January 2000 the near-surface wind speed upstream of the mountains increased further and the wind from the troposphere up to the stratosphere was blowing from the west without any significant directional shear for more than 18 hours (Table 1). Based on mesoscale forecasts of the stratospheric temperature, a flight pattern was chosen in such a way that the mountain-wave-induced temperature anomalies could be observed to a large extent [*Eckermann et al.*, 2002]. Figure 7 depicts the simulated mesoscale temperature distribution at 22 and 26 km, and the flight pattern of the DLR Falcon on this day. The aircraft flew from Kiruna (A, 1315 UT) toward the Norwegian Sea (B, 1335 UT) and on the upstream side along the coast southward (C, 1400 UT). From point C the Falcon flew as far as possible eastward (D, 1500 UT) and turned via Rovaniemi (E, 1535 UT) back to Kiruna (A, 1630 UT). Both cross-mountain flight legs (A-B/E-A and C-D) were aligned with the predicted mean stratospheric wind direction.

[36] The model results shown in Figure 7 are obtained from a mesoscale numerical simulation initialized on 26 January 2000 at 0600 UT. At an elevation of 26 km there are two nearly parallel cold regions with temperatures below 190 K; one is above the mountain ridge and the other is about 500 km downstream over Finland. The north-south extension of the western temperature anomaly is about 650 km, that of the eastern one about 400 km. At 22 km warm regions exist at the cold upper locations indicating an extreme vertical tilt of the mesoscale temperature anomalies.

[37] The observed backscatter ratio γ on the individual flight legs is depicted in Figures 8a and 8b. Here the simulated potential temperatures are superimposed on γ. Upstream, above the Norwegian Sea, there is a thin, only 2-km-thick aerosol layer with $\gamma < 30$ like that observed by NASA's DC-8 the day before (Figure 6). In both cross-mountain flight legs this layer is only slightly undulated, with the most pronounced vertical displacement of about 400 m occurring above the Lofoten archipelago (Figure 8a, top). This is certainly due to vertically propagating gravity waves excited by the flow above isolated mountain peaks (the highest is Storvatnet on Flakstad with an elevation of 932 m) in front of the Scandinavian mountain ridge. On the upstream side the simulated isentropes are nearly parallel (Figure 8b).

[38] In both the northern and the southern cross-mountain flight legs this PSC layer diminishes and vanishes almost in front of the mountains. Directly above the mountains at about 26 km, a PSC layer with backscatter ratios greater than 100 and with a sharp upstream edge has been observed on both flight legs. Along the southern flight leg the whole PSC layer is tilted and extends about 400 km eastward. In its core the backscatter ratio γ is larger than 100, indicating that this is a huge water ice PSC.

[39] The most remarkable feature of the observation along the southern flight leg is the appearance of a second water ice PSC with similar maximum backscatter ratios between 24 and 26 km above Finland. However, its horizontal extension of 100 km is shorter than the western PSC. Between both ice PSCs there is a gap with filamentary aerosol layers flowing out of the western and into the eastern ice PSC.

[40] The simulated isentropes indicate that mountain wave cooling is again the main process responsible for the formation of the observed ice clouds above Scandinavia. The Scandinavian mountain ridge has a sufficient width to excite inertia gravity waves. Due to the action of the Coriolis force, and depending on the horizontal wavelength, their propagation is tilted against the vertical. Therefore they are able to produce significant stratospheric temperature anomalies in the lee of the Scandinavian mountain ridge [*Queney*, 1948; *Gill*, 1982]. The lidar data presented in Figure 8a along the southern flight leg are the first observations that evidently show the influence of inertia gravity waves on the formation of PSCs downstream of the Scandinavian mountain ridge.

[41] The shape of the cloud along the northern flight leg is different. There is no indication of a separated second cloud above Finland. This is in agreement with the simulated temperature structure shown in Figure 7. Along the northern leg the ice cloud above the mountains extends into a nearly horizontal PSC layer. In this layer the backscatter ratio gradually decreases from $\gamma \approx 100$ in the core to smaller values at the upper and lower edges. However, some ice regions still exist about 300 km downstream of the mountains.

[42] A comparison of the upstream and downstream flight legs (Figure 8b) shows that the thin, 2-km-thick PSC layer upstream over the ocean develops into a much thicker (4 km) layer behind the mountains over Finland. Whereas the upstream layer has backscatter ratios of $\gamma < 30$, the downstream layer is less homogeneous and contains isolated patches of high γ values. Upstream and downstream profiles like these contain valuable information for

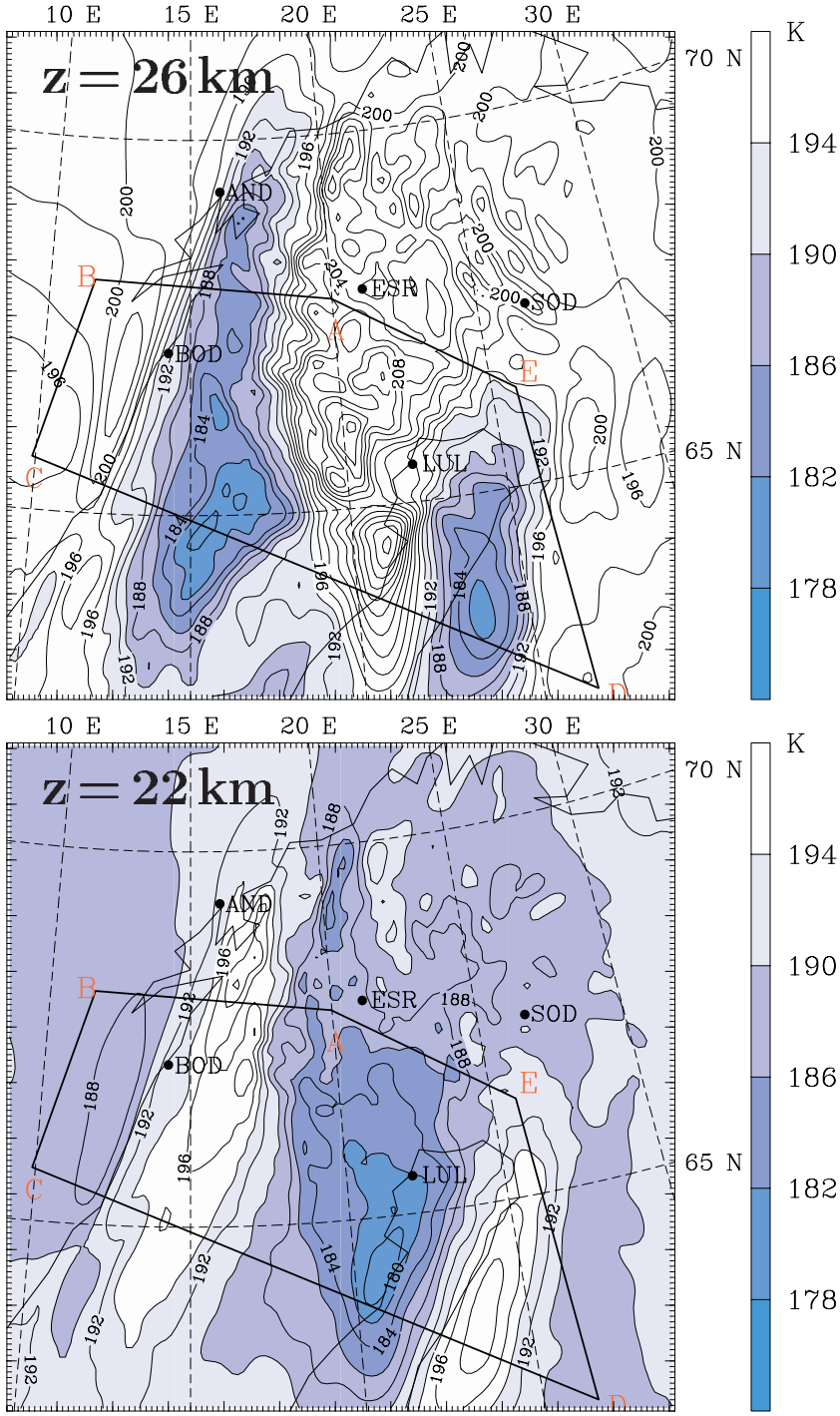

Figure 7. Temperature at 22 and 26 km on 26 January 2000 at 1400 UT (+8 hours). Results from the second model domain (horizontal grid size 8 km) of the MM5 simulation. The flight leg of the DLR Falcon is indicated by a black line, the individual segments are marked by the letters A to E.

verification of satellite observations as done by *Bevilacqua et al.* [in press, 2002].

4.3. Period 27 January 2000

[43] On 27 January 2000 the near-surface wind became weaker (Figure 1 and Table 1) and the core of the polar vortex was located above northern Scandinavia, that is, the stratospheric winds were much smaller (Figures 2 and 3 and Table 1) as well. Therefore the region of significant gravity wave propagation has been shifted with the vortex edge southward (Figure 2).

[44] Figure 9 shows the observed backscatter ratio γ along the flight leg indicated in Figure 3 at two subsequent times. At 1330 UT (Figure 9a) a thin tilted PSC layer is located above the mountain ridge. On its windward side, the infrared backscatter ratio is greater than 100, whereas γ

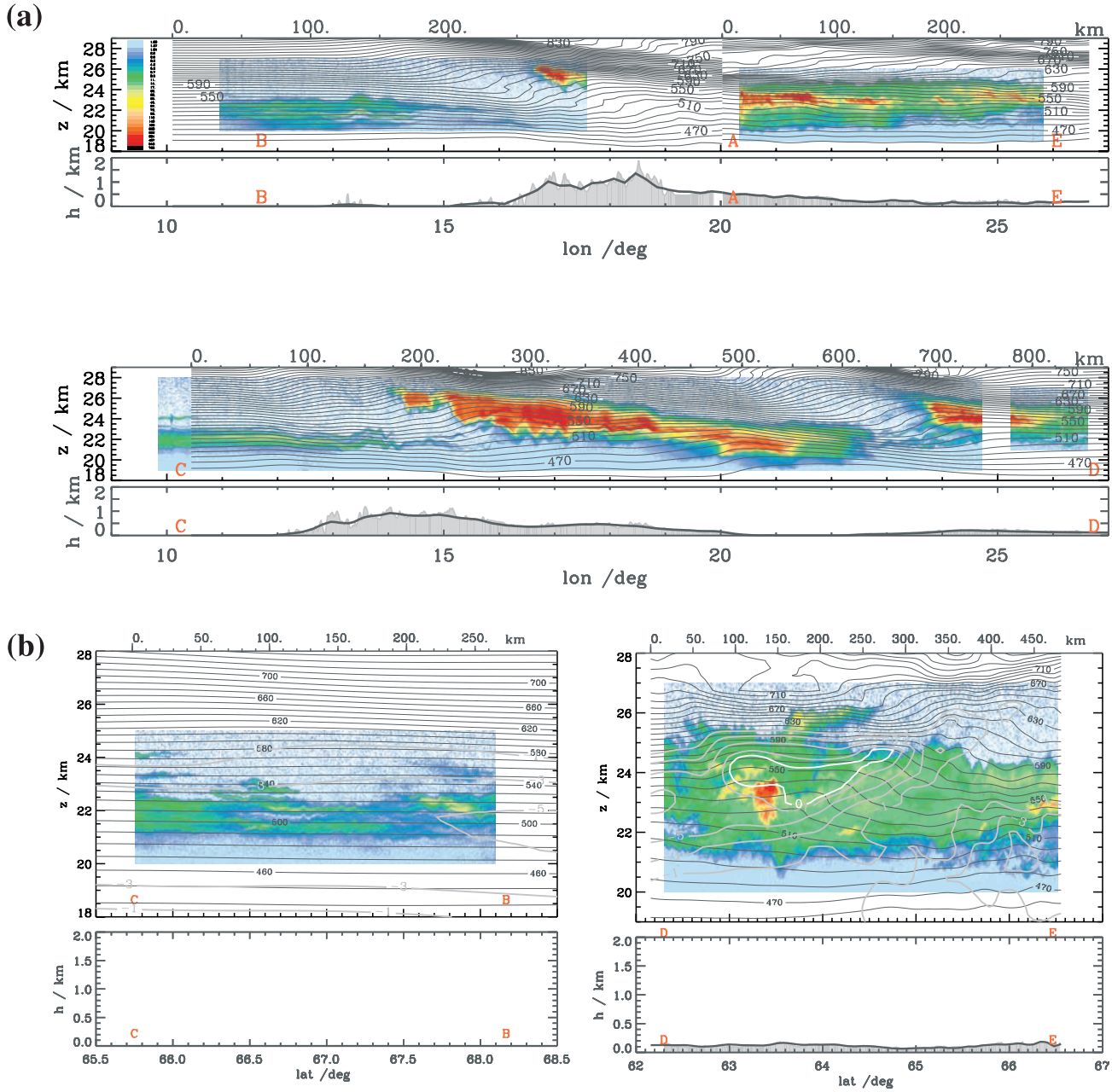

Figure 8. (a) (top) Backscatter ratio γ at 1064 nm along the cross-mountain flight legs of the DLR Falcon on 26 January 2000 (color shading). Superimposed is the MM5 potential temperature along the flight legs at 1400 UT (+8 hours, A–B), 1700 UT (+11 hours, E–A), and 1400 UT (+8 hours, C–D). (bottom) As in Figure 5. (b) Backscatter ratio γ at 1064 nm along the (left) upstream and (right) downstream flight legs of the DLR Falcon on 26 January 2000 (color shading). Superimposed is the MM5 potential temperature along the flight tracks at 1300 UT (+7 hours, B–C) and 1500 UT (+9 hours, D–E). The white lines denote the local deviation $T - T_{\text{frost}}$, and the gray lines denote $T - T_{\text{NAT}}$. The PSC formation temperatures T_{NAT} and T_{frost} are calculated assuming volume mixing ratios of 5 ppm for water vapor and 10 ppb for NAT [*Hanson and Mauersberger*, 1988].

decreases gradually in the downwind tail. Just 1 hour later (Figure 9b) only a small patch of the ice cloud directly above the mountain peaks remained; the residual of the cloud has almost disappeared. The superimposed isentropes of the mesoscale simulation identify a vertically propagating gravity wave of small amplitude as the source of the local stratospheric temperature reduction. Since the excitation of the mountain waves is reduced during the day, the wave amplitude diminishes and the local stratospheric cooling by waves ceases (Figure 9).

5. Classification of PSC Types

[45] So far only the thermodynamic properties of the observed clouds have been discussed. Next, we present a classification of cloud composition in terms of optical

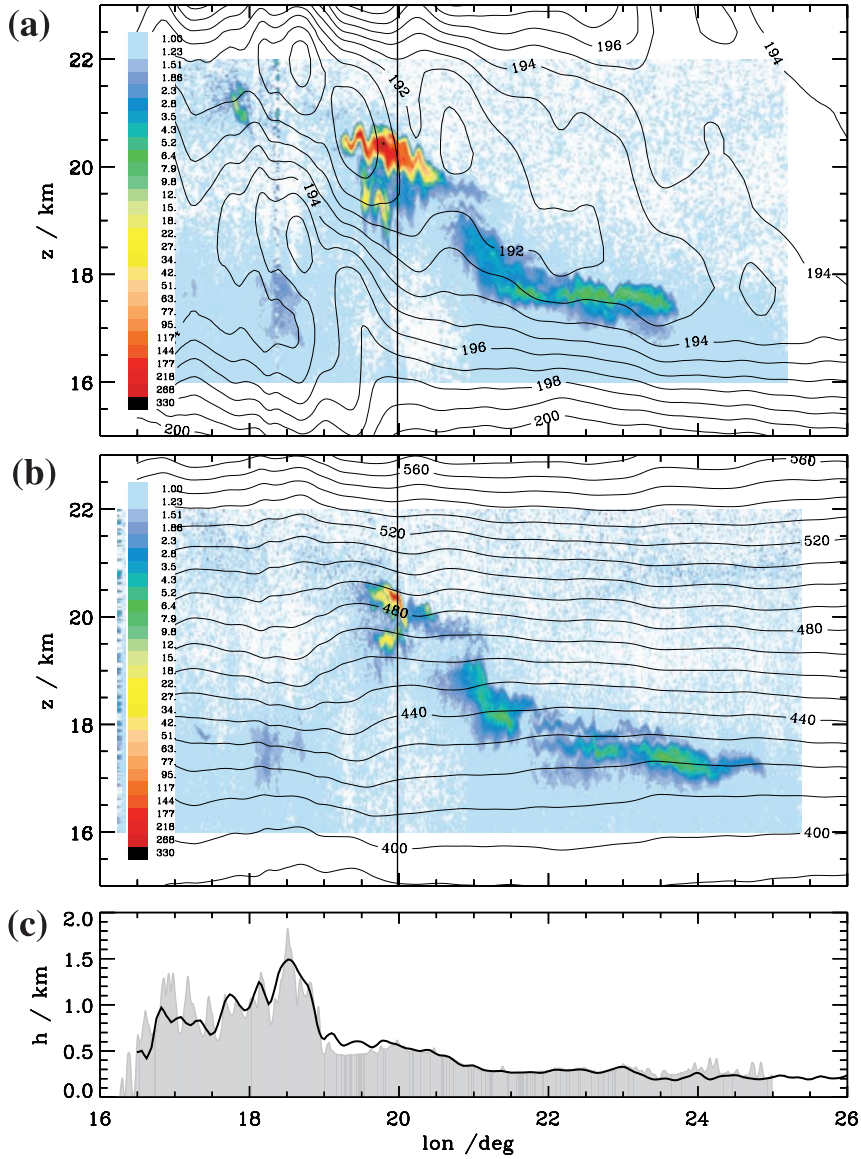

Figure 9. (a) Backscatter ratio γ at 1064 nm along two flight legs of the DLR Falcon on 27 January 2000 from 1315 UT to 1330 UT and (b) on same flight path 1 hour later. Superimposed are the MM5 temperature (1 K interval) and potential temperature (10 K interval) along the flight track at 1400 UT (+8 hours). The vertical line marks the position of Kiruna. (c) As in Figure 5.

properties measured by the lidar instrument (Figure 10). The classification is based on the backscatter ratios γ_λ at λ = 1064 and 532 nm and on the depolarization δ_{532} at 532 nm. Although the infrared depolarization is not available for the OLEX measurements a similar classification scheme as that proposed by *Browell et al.* [1998] is applied. For minimum backscatter ratio for all PSC types, $\gamma_{1064} > 1.6$ and $\gamma_{532} > 1.17$. For depolarization $\delta_{532} > 4.0\%$, PSC type II (water ice particles) $\gamma_{1064} > 21.0$ and $\gamma_{532} > 10.0$, PSC type Ia-enhanced (small NAT particles); $5.0 < \gamma_{1064} < 26.0$ and $1.5 < \gamma_{532} < 10.0$, PSC type Ia (solid NAT particles); $\gamma_{1064} < 5.0$ and $\gamma_{532} < 1.5$. For depolarization $\delta_{532} < 4.0\%$, PSC type Ib (liquid STS droplets).

[46] Stratospheric clouds consist of particle mixtures with different phases and compositions [*Schreiner et al.*, 1999; *Carslaw et al.*, 1999; *Tsias et al.*, 1999; *Larsen et al.*, 2000]. It should be noted that the above empirical classification is dominated by strongly backscattering and depolarizing particles. Therefore mixed areas are always classified corresponding to their optically most effective particles. Areas not assignable to one of the classes are left white in Figure 10.

[47] According to the above classification scheme, the core of the PSC observed by DLR Falcon on 25 January consists of water ice particles (see Figure 10, top). Upstream of the ice cloud, thin filaments of liquid STS droplets are identified. In these filaments a few patches of small NAT particles are classified. The layer at the upper edge of the ice cloud is dominated by liquid STS. However, there is a sharp phase transition along the vertical from water ice particles to liquid STS droplets with possible NAT patches in between. At the lower edge of the observed cloud a mixture of small NAT particles and STS droplets exists. The downwind tail

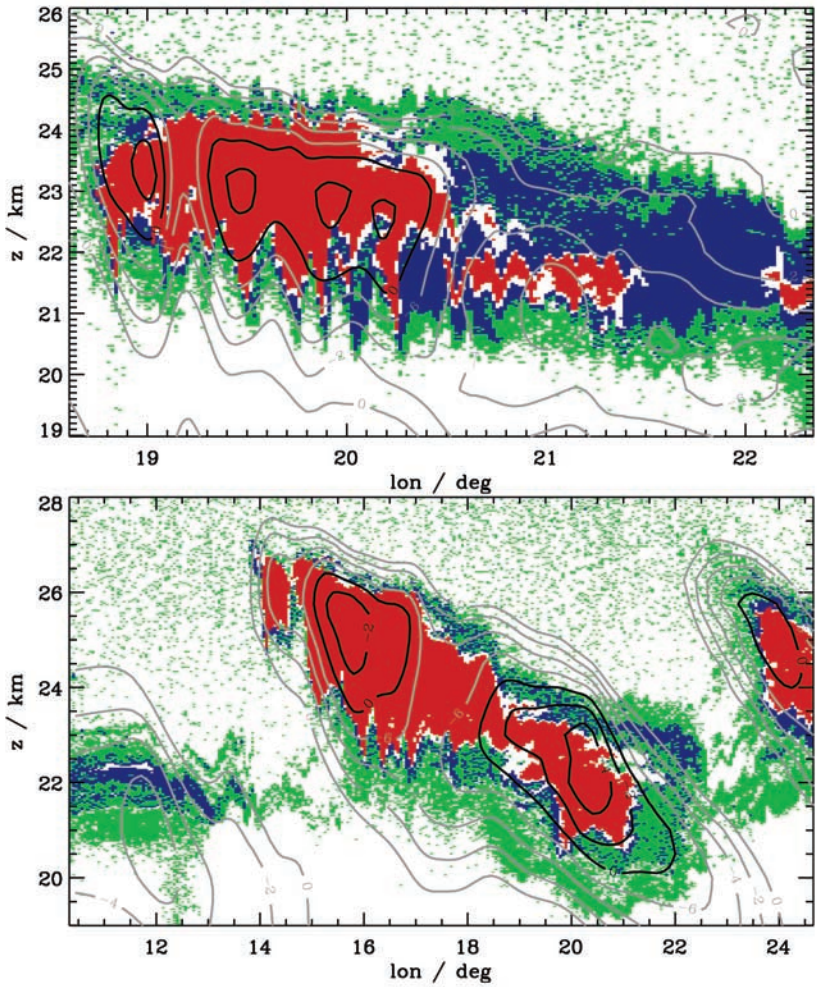

Figure 10. Classification of PSC particles from the observations on (top) 25 January and (bottom) 26 January 2000; see Figures 5 and 8a. Color shading: red, water ice particles (PSCs of type II); light blue, solid NAT particles ($HNO_3 - 3 \cdot H_2O$; PSCs of type Ia); dark blue, small NAT particles (PSCs of type Ia enhanced); green, liquid supercooled ternary solutions ($HNO_3/H_2SO_4/H_2O$; PSCs of type Ib). For classification algorithm see text. Superimposed are temperature anomalies from the mesoscale simulations: black lines, local deviation $T - T_{frost}$; gray lines, $T - T_{NAT}$. The PSC formation temperatures T_{NAT} and T_{frost} are calculated assuming volume mixing ratios of 5 ppm for water vapor and 10 ppb for NAT [*Hanson and Mauersberger*, 1988].

of the cloud is dominated by small NAT particles according to the above classification.

[48] In Figure 10 the simulated local temperature deviations $T - T_{frost}$ and $T - T_{NAT}$ are superimposed on the optical classification of PSC particles for both flight legs. On 25 January, all backscattering particles are in regions where the simulated temperature is more than 2 K below T_{NAT}. Regions with $T - T_{frost} < 0$ are located in the core of the ice cloud whereby a maximum deviation of −2.7 K was simulated at 23.2 km altitude and at 19 E. The sharp phase transition at the upper edge of the cloud is well simulated in terms of drastically increasing temperatures along the vertical.

[49] The classification of the PSC observed by NASA DC-8 DIAL (Figure 6) a few hours later shows some remarkable similarities to the former classification. PSC classifications made using data from both instruments converge on the conclusion that the ice cloud is surrounded by NAT particles. These particles also dominate the downwind tail in both observations. Furthermore, along both flight legs downstream of the mountains there are a few isolated thin ice layers at ≈21 km embedded in the NAT particles. However, in the OLEX classification a layer of liquid STS droplets about 500 m thick dominates the upper edge of the ice cloud, whereas the observation by NASA DC-8 DIAL identifies only small areas of liquid aerosols. At the lower edge, layers of small NAT particles and liquid STS droplets have been classified correspondingly by both observations.

[50] On 26 January 2000 the formation of ice particles starts more abruptly at the windward edge of the cloud compared to the PSC observed on the day before (Figure 10, bottom). Along the head of the long ice cloud there is only a thin coat of a mixture of liquid STS droplets and

small NAT particles. Downwind, east of 18°E, and due to warmer temperatures at lower altitude, the layer depth of the mixed phases grows. In contrast to the cloud on 25 January 2000 the lidar observation identifies mainly liquid STS droplets on the lee side of this PSC. A tail of small NAT particles occurs only at the upper downwind levels at about 24 km. The transition to the second cloud above Finland is characterized by thin filaments of liquid STS droplets. In agreement with the simulated temperature distribution these filaments form only at lower levels where the air is too warm for the creation of ice PSCs, but not so warm as to quickly evaporate the ice aerosols. Because of these preprocessed particles, the phase transition from liquid aerosol droplets occurs more gradually toward water ice particles in front of the easterly PSC. The shape of the huge ice clouds corresponds to regions where $T - T_{NAT} < -4$ K. In the interior the temperature falls as much as 5.8 K (13.7 K) below T_{frost} (T_{NAT}) at 22 km altitude at 20.4°E. Generally, the simulated areas of $T < T_{NAT}$ are in concordance with the overall shape of the observed PSCs.

[51] On the upstream side of the mountains, that is, west of 14°E, the synoptic-scale PSC consists of small NAT particles near 22 km embedded in STS droplets between 21 and 23 km. Again, this PSC region is similar to the location of minimum temperatures simulated by the mesoscale model. Here the temperature falls as much as 6 K below T_{NAT} and the particles begin to evaporate in regions where $T - T_{NAT}$ becomes greater than -4 K in the region from 13° to 15°E. The DC-8 classification of a similar upstream PSC layer from 25 January, as composed of liquid STS and small NAT particles, agrees with this OLEX classification.

6. Discussion

[52] This paper presents lidar observations of polar stratospheric clouds during a 3-day period characterized by significant mountain wave activity above northern Scandinavia. During this period, the synoptic tropospheric situation was dominated by an eastward traveling depression north of Scandinavia. Further south a stationary high-pressure system was situated over the Atlantic Ocean. Between the cyclonic and the anticyclonic pressure systems a strong westerly flow past the Scandinavian mountain range developed (Figure 1). This flow excited internal gravity waves that were able to propagate up into the stratosphere. The correlation of blocking highs [*Brezowsky et al.*, 1951] with the appearance of PSCs above northern Scandinavia was noted early on by *Dietrichs* [1950].

[53] On 25 January 2000, significant adiabatic cooling in steep hydrostatic gravity waves with horizontal wavelenghs of about 30 km formed ice PSCs between 20 and 24 km altitude above the mountains. These PSCs were observed by aerosol backscatter lidars on board the DLR Falcon and the NASA DC8 (Figures 5 and 6). The elevation of the mountain-wave-induced PSC was only slightly higher than that of the synoptic-scale PSC upstream of the mountains. However, the localized cooling produced a broader spectrum of aerosol particles in terms of composition and size distribution [*Voigt et al.*, 2000; *Schreiner et al.*, 2002; *Larsen et al.*, 2002].

[54] The simulated isentropes overturn above the cloud. This wave breaking prevented the further vertical propagation of mountain waves. Since all the wave energy is trapped below the self-induced critical level, the observed nearly horizontal ice PSC layer downstream of the mountains could form. The mesoscale model simulations correlate well with the observed position of ice formation and with the measured wave amplitudes. Even smaller scale features resulting from individual mountain peaks could be reproduced by the mesoscale model simulation having a minimum horizontal resolution of 2.67 km (see Figure 6).

[55] On 26 January 2000, longer hydrostatic gravity waves were excited by the long-lasting flow across the mountains. Due to the position of the polar vortex directly above northern Scandinavia these waves propagated without significant absorption into the stratosphere where they generated mesoscale temperature anomalies downstream of the mountain ridge. Except for the upstream synoptic-scale PSC, the observations of this day show marked differences from the former PSC. The ice cloud covers a height range between 20 and 27 km and extends more than 400 km along the mean wind direction. The DLR Falcon observation of a second, separated stratospheric ice cloud gives strong evidence for localized stratospheric ice clouds generated by inertia gravity waves far downstream of their launch region. The long-lasting flow past the wide mountain range is a necessary prerequisite for the formation of these clouds, because of the longer propagation time compared to the clouds formed by the shorter vertically propagating waves [*Dörnbrack et al.*, 1999]. The propagation time of a gravity wave from the surface to an altitude of $z = 26$ km can be estimated by $t_p = z/c_{gz}$, where the vertical component of the group velocity c_{gz} for hydrostatic mountain waves in the nonrotating regime is given by

$$c_{gz} = \frac{\omega^2}{N k_H} = \frac{V_H^2 k_H}{N},$$

where $k_H = 2\pi/\lambda_H$ is the horizontal component of the wave vector [*Gill*, 1982, chapter 8.4], ω is the intrinsic frequency, V_H is the horizontal wind speed, and the buoyancy frequency is $N = \sqrt{g/\vartheta d\vartheta/dz}$, where ϑ is the potential temperature. For mean conditions $N = 0.02$ s^{-1} and $V_H = 30$ m s^{-1}, and the propagation time t_p for waves of $\lambda_H \approx 50$ km is about 1.4 hours. The horizontal wavelength of the mountain waves in Figure 8a is about 400 km, that is, $t_p \approx$ 12 hours. The modification of the vertical group velocity c_{gz} for long hydrostatic mountain waves in the rotating regime is less than 12% for $\lambda_H < 400$ km [*Dörnbrack et al.*, 1999].

[56] The observation of a thin attenuating PSC layer on 27 January 2000 is correlated with diminishing tropospheric excitation and the southward propagation of the edge of the polar vortex (Figures 2 and 3). This confirms the close correlation of stratospheric wave energy maxima with the position of the polar vortex and is in accordance with recent observations above Canada [*Whiteway et al.*, 1997; *Whiteway and Duck*, 1999] which found marked stratospheric temperature anomalies correlated with the position of the edge of the Arctic polar vortex.

[57] The types of the different cloud particles have been classified in terms of the optical properties of the backscattered lidar signal. The core of the observed clouds on 25 and 26 January 2000 consists of strongly scattering ice particles which agrees with the simulated temperatures up to 5 K below the frost point in these areas. Small NAT

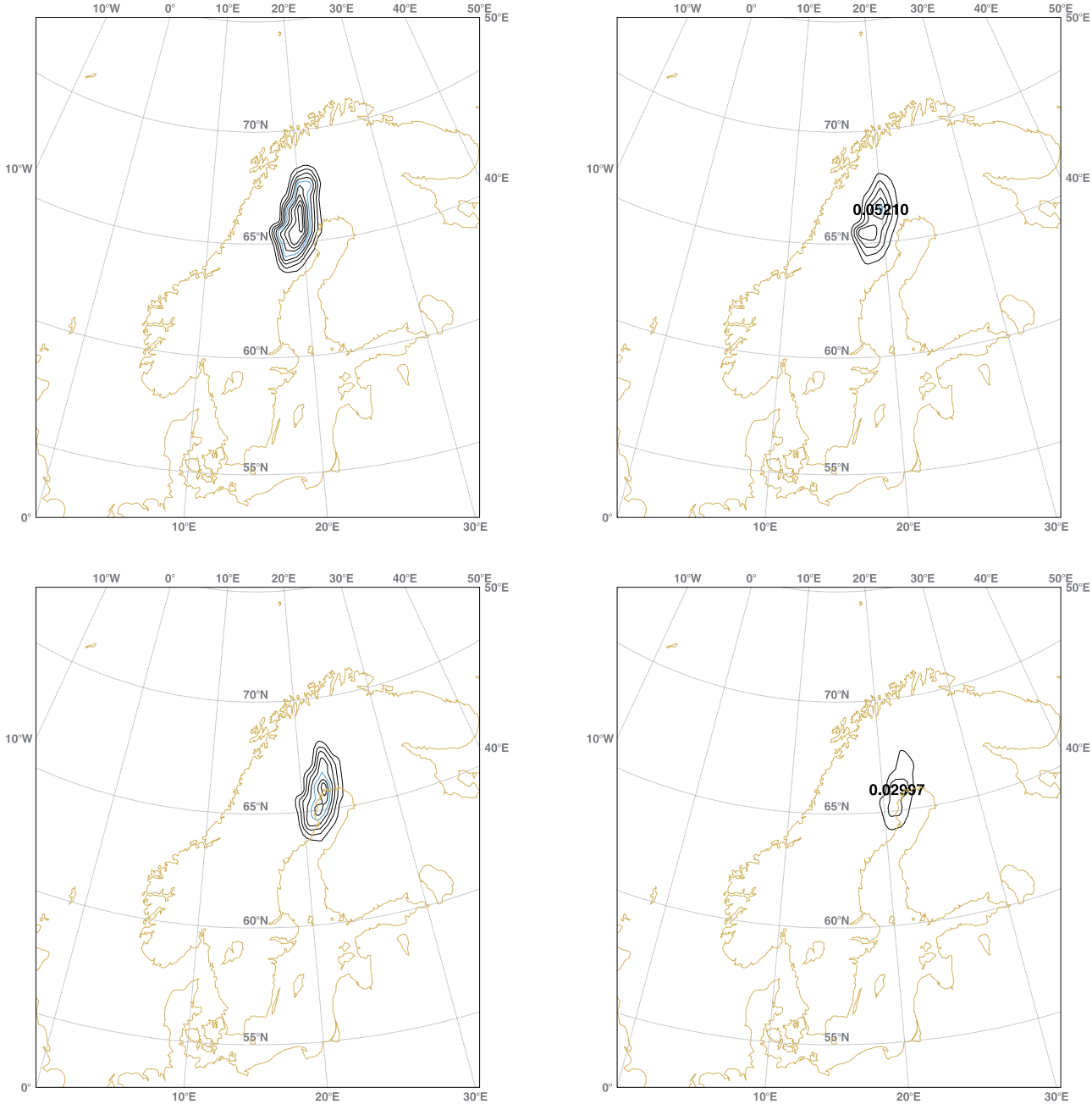

Figure 11. (left) Cloud cover (percent) on the stratospheric model levels 17 (top, 18.8 hPa, ≈26. . .28 km) and 19 (bottom, 28.8 hPa, ≈23. . .25 km) on 26 January 2000 at 1200 UT. (right) Cloud water ice content (10^{-6} kg kg^{-1}) on the same levels and date. The fields are results of the +6 hours first guess of the ECMWF analyses at a horizontal resolution of 0.5° × 0.5°.

particles and liquid STS droplets are solely identified at the boundaries of the clouds. On 25 January the downwind tail of the ice cloud has a complex composition but is dominated by small NAT particles. There the simulated temperature varies between 187 and 192 K and explains a broad complexity of particle occurrence, phase, and composition. Furthermore, this classification is in agreement with observations of an independent lidar instrument flown on NASA's DC-8 and with the in situ observations of *Voigt et al.* [2000] who found NAT particles near, and even above, their equilibrium temperature on that day about 300 km downstream of the Scandinavian mountain ridge. An interesting fact is that only very small areas of large NAT particles are found. This may be due to the short time (a few hours) available for the particle to grow to larger sizes in these clouds. In contrast to the NAT-tail of the ice cloud on 25 January the same classification results in a tail of liquid STS droplets 1 day later, possibly due to the strong increase of temperature along the streamlines as suggested by the mesoscale model results (Figures 7 and 8a).

[58] As described in section 5 this empirical classification of the PSC particles is mainly based on the values of the

total backscatter ratio in the infrared and visible channel and on the aerosol depolarization of the visible laser signal. This classification will be confirmed and complemented by means of T-Matrix calculations [*Carslaw et al.*, 1998b; *Mishchenko*, 1991] and by microphysical modeling in further publications [*Larsen et al.*, 2002; *Schreiner et al.*, 2002].

[59] As documented in Figure 3, and recently by *Eckermann et al.* [2002] and *Kivi et al.* [2001], the recent ECMWF analyses are able to reproduce mountain-wave-induced temperature anomalies above the Scandinavian mountain ridge. The peak-to-peak amplitude of 15 K is smaller than that of the mesoscale simulations (36 K) presented in Figure 7. Nevertheless, due to additional stratospheric levels and the increase of spatial resolution, the current global ECMWF weather forecast model opens the opportunity to consider processes at scales that formerly were not resolved. In Figure 11, the +6 hours first guess analyses of the cloud cover and the cloud water ice content are shown for two stratospheric model levels valid at 1200 UT on 26 January 2000.

[60] Obviously, the ECMWF analyses generate a stratospheric ice cloud at the same position as observed. Also the observed vertical tilt is well represented. However, the observed second PSC does not appear in the analysis. As shown in section 4, the eastern stratospheric temperature above Finland was generated by long hydrostatic gravity waves. The propagation time to an altitude of 25 km was estimated to be about 10 hours. Therefore the forecast time of +6 hours is too short to allow longer waves to propagate up to the stratosphere, and the downstream mesoscale temperature anomaly could not be calculated. Thus observations and mesoscale modeling as presented in this paper should be utilized to test the global model predictions. Additionally, further work is needed to adjust the parametrizations of stratospheric cloud formation processes to observed reality or to mesoscale simulations in concert with microphysical modeling. This remains a task for future work.

[61] **Acknowledgments.** The aircraft flights were performed as part of the American-European SOLVE/THESEO-2000 campaign in the winter of 1999/2000. This work has been supported by the Commission of the European Union through the Environment and Climate program (contract EVK2-CT-1999-00047). The ECMWF data were available through the special project "Effect of nonhydrostatic gravity waves on the stratosphere above Scandinavia" by one of the authors (A.D.). We appreciate the collaboration with Günther Zängl who helped to implement his modified upper boundary condition in our MM5 version. The computations were performed on the NEC-SX5 of DLR Braunschweig. We thank Andreas Landhäußer for his cooperation and John G. Michalakes for his parallelized version of the MM5 code for NEC-SX5. Most of the paper was written while one of the authors was visiting the Finnish Meteorological Institute in January 2001. A.D. thanks very much Esko Kyrö and Rigel Kivi for the excellent working conditions at Sodankylä.

References

Baines, P. G., *Topographic Effects in Stratified Flows*, 482 pp., Cambridge Univ. Press, New York, 1995.

Bevilacqua, R. M., et al., Observations and analysis of polar stratospheric clouds detected by POAM III during the 1999/2000 Northern Hemisphere winter, *J. Geophys. Res.*, *107*, doi:10.1029/2001JD000477, in press, 2002.

Booker, J. R., and F. P. Bretherton, The critical layer for internal gravity waves in a shear flow, *J. Fluid Mech.*, *27*, 513–539, 1967.

Brezowsky, H., H. Flohn, and P. Hess, Some remarks on the climatology of blocking action, *Tellus*, *3*, 191–194, 1951.

Browell, E. V., S. Ismail, and W. B. Grant, Differential absorption lidar (DIAL) measurements from air and space, *Appl. Phys. B*, *67*, 399–410, 1998.

Carslaw, K. S., et al., Increased stratospheric ozone depletion due to mountain-induced atmospheric waves, *Nature*, *391*, 675–678, 1998a.

Carslaw, K. S., M. Wirth, A. Tsias, B. P. Luo, A. Dörnbrack, M. Leutbecher, H. Volkert, W. Renger, J. T. Bacmeister, and T. Peter, Particle microphysics and chemistry in remotely observed mountain polar stratospheric clouds, *J. Geophys. Res.*, *103*, 5785–5796, 1998b.

Carslaw, K. S., T. Peter, J. T. Bacmeister, and S. D. Eckermann, Widespread solid particle formation by mountain waves in the Arctic stratosphere, *J. Geophys. Res.*, *104*, 1827–1836, 1999.

Dietrichs, H., Über die Entstehung der Perlmutterwolken, *Meteorol. Rundsch.*, *3*, 208–213, 1950.

Dörnbrack, A., M. Leutbecher, R. Kivi, and E. Kyrö, Mountain wave induced record low stratospheric temperatures above northern Scandinavia, *Tellus*, *51A*, 951–963, 1999.

Dörnbrack, A., M. Leutbecher, J. Reichardt, A. Behrendt, K. P. Müller, and G. Baumgarten, Relevance of mountain wave cooling for the formation of polar stratospheric clouds over Scandinavia: Mesoscale dynamics and observations for January 1997, *J. Geophys. Res.*, *106*, 1569–1582, 2001.

Dudhia, J., A nonhydrostatic version of the Penn State–NCAR Mesoscale Model: Validation tests and simulation of an Atlantic cyclone and cold front, *Mon. Weather Rev.*, *121*, 1493–1513, 1993.

Dudhia, J., D. Gill, Y.-R. Guo, K. Manning, and W. Wang, PSU/NCAR Mesoscale Modeling System Tutorial Class Notes and User Guide: MM5 Modeling System Version 3, NCAR, Boulder, Colo., 2001. (Also at www.mmm.ucar.edu/mm5/doc.html).

Eckermann, S. D., A. Dörnbrack, S. B. Vosper, and K. S. Carslaw, Mesoscale forecasting of the stratosphere during SOLVE-THESEO 2000, *J. Geophys. Res.*, 2002.

Enell, C., Å. Steen, T. Wagner, U. Frieß, K. Pfeilsticker, U. Platt, and K.-H. Fricke, Occurrence of polar stratospheric clouds at Kiruna, *Ann. Geophys.*, *17*, 1457–1462, 1999.

Flentje, H., W. Renger, M. Wirth, and W. A. Lahoz, Validation of contour advection simulations with airborne lidar measurements of filaments during the Second European Stratospheric Arctic and Midlatitude Experiment (SESAME), *J. Geophys. Res.*, *105*, 15,417–15,437, 2000.

Gary, B. L., Observational results using the microwave temperature profiler during the airborne Antarctic ozone experiment, *J. Geophys. Res.*, *94*, 11,223–11,231, 1989.

Gill, A. E., *Atmosphere-Ocean Dynamics*, 662 pp., Academic, San Diego, Calif., 1982.

Grant, W. B., M. A. Fenn, E. V. Browell, T. J. McGee, U. N. Singh, M. R. Gross, I. S. McDermid, L. Froidevaux, and P.-H. Wang, Correlative stratospheric ozone measurements with the airborne UV DIAL system during TOTE/VOTE, *Geophys. Res. Lett.*, *25*, 623–626, 1998.

Hanson, D., and K. Mauersberger, Laboratory studies of the nitric acid trihydrate: Implications for the south polar stratosphere, *Geophys. Res. Lett.*, *15*, 855–858, 1988.

Kivi, R., E. Kyrö, A. Dörnbrack, and T. Birner, Observations of vertically thick polar stratospheric clouds and record low temperature in the Arctic vortex, *Geophys. Res. Lett.*, *28*, 3661–3664, 2001.

Klett, J. D., Lidar inversion with variable backscatter/extinction ratios, *J. Appl. Opt.*, *24*, 1638–1643, 1985.

Larsen, N., I. S. Mikkelsen, B. M. Knudsen, J. Schreiner, C. Voigt, K. Mauersberger, J. M. Rosen, and N. T. Kjome, Comparison of chemical and optical in situ measurements of polar stratospheric clouds, *J. Geophys. Res.*, *105*, 1491–1502, 2000.

Larsen, N., et al., Microphysical mesoscale simulations of polar stratospheric cloud formation over northern Scandinavia on 25 January 2000 constrained by in situ measurements of chemical and optical cloud properties, *J. Geophys. Res.*, *107*, doi:10.1029/2001JD000999, in press, 2002.

Manney, G. L., and J. L. Sabutis, Development of the polar vortex in the 1999–2000 Arctic winter stratosphere, *Geophys. Res. Lett.*, *27*, 2589–2592, 2000.

Mishchenko, M. I., Light scattering by randomly oriented axially symmetric particles, *J. Opt. Soc. Am.*, *8*, 871–882, 1991.

Moerl, P., M. E. Reinhardt, W. Renger, and R. Schellhase, The use of the airborne lidar system "ALEX F1" for aerosol tracing in the lower troposphere, *Contrib. Atmos. Phys.*, *54*, 401–410, 1981.

Pawson, S., B. Naujokat, and K. Labitzke, On the polar stratospheric cloud formation potential of the northern stratosphere, *J. Geophys. Res.*, *100*, 23,215–23,225, 1995.

Peter, T., Microphysics and heterogeneous chemistry of polar stratospheric clouds, *Annu. Rev. Phys. Chem.*, *48*, 785–822, 1997.

Queney, P., The problem of airflow over mountains: A summary of theoretical studies, *Bull. Am. Meteorol. Soc.*, *29*, 16–27, 1948.

Schiller, C., et al., Dehydration in the Arctic stratosphere during the THE-

SEO-2000/SOLVE campaigns, *J. Geophys. Res.*, *107*, doi:10.1029/2001JD000463, in press, 2002.
Schreiner, J., C. Voigt, A. Kohlmann, F. Arnold, K. Mauersberger, and N. Larsen, Chemical analysis of polar stratospheric cloud particles, *Science*, *283*, 968–970, 1999.
Schreiner, J., et al., Chemical, microphysical and optical properties of polar stratospheric clouds, *J. Geophys. Res.*, in press, 2002.
Störmer, C., Remarkable clouds at high altitudes, *Nature*, *123*, 940–941, 1929.
Störmer, C., Höhenmessungen von Stratosphärenwolken, *Beitr. Phys. Atmos.*, *21*, 1–6, 1934.
Tsias, A., et al., Aircraft observations of an enhanced type Ia polar stratospheric cloud during APE-POLECAT, *J. Geophys. Res.*, *104*, 23,961–23,969, 1999.
Voigt, C., et al., Nitric acid trihydrate (NAT) in polar stratospheric clouds, *Science*, *290*, 1756–1758, 2000.
Whiteway, J. A., and T. J. Duck, Enhanced Arctic stratospheric gravity wave activity above a tropospheric jet, *Geophys. Res. Lett.*, *26*, 2453–2456, 1999.
Whiteway, J. A., T. J. Duck, D. P. Donovan, J. C. Bird, S. R. Pal, and A. I. Carswell, Measurements of gravity wave activity within and around the Arctic stratospheric vortex, *Geophys. Res. Lett.*, *24*, 1387–1390, 1997.
Wirth, M., and W. Renger, Evidence of large-scale ozone depletion within the Arctic polar vortex 94/95 based on airborne LIDAR measurements, *Geophys. Res. Lett.*, *23*, 813–816, 1996.
Wirth, M., A. Tsias, A. Dörnbrack, V. Weiß, K. S. Carslaw, M. Leutbecher, W. Renger, H. Volkert, and T. Peter, Model guided Lagrangian observation and simulation of mountain polar stratospheric clouds, *J. Geophys. Res.*, *104*, 23,971–23,981, 1999.
World Meteorological Organization, Scientific assessment of ozone depletion: 1998, *Rep. 44*, Geneva, 1999.
Zängl, G., Stratified flow over a mountain with a gap, I, Linear regime, *Q. J. R. Meteorol. Soc.*, *128*, 927–950, 2002.

T. Birner and A. Dörnbrack, DLR Oberpfaffenhofen, Institut für Physik der Atmosphäre, D-82230 Wessling, Germany. (thomas.birner@dlr.de; andreas.doernbrack@dlr.de)

E. V. Browell, Lidar Application Group, Atmospheric Science Research, NASA Langley Research Center, M.S. 401A, Hampton, VA 23681-0001, USA. (e.v.browell@larc.nasa.gov)

A. Fix, H. Flentje, A. Meister, and H. Schmid, DLR Oberpfaffenhofen, Lidar Gruppe, D-82230 Wessling, Germany. (andreas.fix@dlr.de; harald.flentje@dlr.de; alexander.meister@dlr.de; heidi.schmid@dlr.de)

M. J. Mahoney, Jet Propulsion Laboratory, California Institute of Technology, 4800 Oak Grove Drive, M.S. 246-101, Pasadena, CA 91109-8099, USA. (m.j.mahoney@jpl.nasa.gov)